

**Two-dimensional multiferroics in a breathing kagome lattice**

Yongchang Li, Chang Liu, Guo-Dong Zhao, Tao Hu, and Wei Ren\*

*Physics Department, State Key Laboratory of Advanced Special Steel, Shanghai Key Laboratory of Advanced Ferrometallurgy, Shanghai University, Shanghai 200444, China**and Materials Genome Institute, International Center of Quantum and Molecular Structures, and Shanghai Key Laboratory of High Temperature Superconductors, Shanghai University, Shanghai 200444, China*

(Received 26 July 2020; revised 22 January 2021; accepted 14 July 2021; published 5 August 2021)

Geometric frustrated kagome systems can show complex and exotic magnetic properties. We theoretically predict ways in which these can be manipulated in two-dimensional (2D) multiferroic materials from first-principles density functional theory calculations. We propose that  $\text{Ti}_3\text{X}_8$  ( $X = \text{Br}$  or  $\text{I}$ ) compounds are shown to form 2D intrinsic semiconductors with breathing kagome lattices containing coexisting ferroelectric (FE) and ferromagnetic ordering. Inside the lattice, Ti atoms distort from high-symmetry locations to produce trimers with shorter interatomic distances that form the basis of local cluster magnets. Lattice breathing interchanges trimer patterns, switching the direction of out-of-plane FE polarization while simultaneously rearranging the interactions between the cluster magnets. FE switching of the monolayer  $\text{Ti}_3\text{X}_8$ , which is concomitant with the direction reversal of the vector of the Dzyaloshinskii-Moriya interaction, is feasible to be manipulated by the application of out-of-plane electric fields. Through the interlayer interaction, the coupling of FE and magnetism is achieved in bilayer  $\text{Ti}_3\text{I}_8$ . The magnetic configurations are transformed between interlayer ferromagnetism and antiferromagnetism by switching the FE polarization directions of bilayer  $\text{Ti}_3\text{I}_8$ . Our findings expand the arena for realizing 2D multiferroics and magnetoelectric effect.

DOI: [10.1103/PhysRevB.104.L060405](https://doi.org/10.1103/PhysRevB.104.L060405)**I. INTRODUCTION**

Quantum materials with two or more coexisting ferroic orders, known as multiferroics, are promising candidates for next-generation spintronic devices, owing to their rich and functional properties [1–5]. The most attractive types of multiferroics for information-technology applications are those made by combining ferroelectricity (FE) and ferromagnetism (FM) either in single-phase structures or in heterostructures. Indeed, controlling FM using an external electric field, or controlling FE polarization using an external magnetic field, may lead to applications of FM/FE multiferroics for memory and logic devices. However, the mutually exclusive origin of FM and FE makes multiferroics in single phase challenging. The perovskite oxides  $\text{BiFeO}_3$  and  $\text{TbMnO}_3$  form three-dimensional (3D) multiferroics that have been extensively studied [6–11]. Some quasi-one-dimensional (1D) systems with strong magnetoelectric coupling have also been studied [12,13]. Due to more restrictions in ultrathin films, such as depolarization field, intrinsic two-dimensional (2D) multiferroic materials were rarely discovered. Recently, breakthroughs have been made in establishing both 2D FM and FE. For instance, 2D FM was experimentally observed in the  $\text{CrI}_3$  and the  $\text{Cr}_2\text{Ge}_2\text{Te}_6$  [14,15]. Moreover, 2D FE was also discovered in atomic thick structures such as  $\text{SnTe}$  [16],  $\text{CuInP}_2\text{S}_6$  [16,17], and  $\text{In}_2\text{Se}_3$  [18,19]. These exciting progresses indi-

cate the possibility of realizing experimentally intrinsic 2D multiferroics.

The compound  $\text{NaSr}_2\text{V}_3\text{O}_3(\text{Ge}_4\text{O}_{13})\text{Cl}$  is a 3D material with interesting electronic and magnetic properties [20]. Both electric polarity and magnetism in this complicated solid can be attributed to isolated internal  $\text{V}_3\text{O}_{13}$  units formed by three edge-sharing distorted  $\text{VO}_6$  octahedra. The same polar structural units have also been observed in  $AM_3X_8$  ( $A =$  interstitial cations,  $M =$  transition metals, and  $X =$  anions) compounds. Of particular significance is that, in the spin- $\frac{1}{2}$   $\text{LiZn}_2\text{Mo}_3\text{O}_8$  system, analogous trimer cluster  $\text{Mo}_3\text{O}_{13}$  units [see Fig. 1(a)] are connected with each other to form 2D  $\text{Mo}_3\text{O}_8$  layers [21–25]. The trimeric cluster units are connected, forming a “breathing” kagome lattice wherein the up ( $\Delta$ ) and down ( $\nabla$ ) triangles are of different size, as shown in Fig. 1(b). The size differential leads to local electric dipole moments that are FE ordered. Also, the unpaired  $d$  electrons on each Mo ion interact strongly within the smaller triangular clusters, leading to net local magnetic moments associated with each cluster. The process of “breathing” refers to vibrations or chemical reactions inside the 2D material that interchange the smaller and larger clusters. This process will clearly modulate both FE and FM properties of the 2D material. Breathing kagome lattices of this type have also been observed in van der Waals (vdW) layered  $\text{Nb}_3\text{X}_8$  ( $X = \text{Cl}, \text{Br},$  or  $\text{I}$ ) material and in a low-temperature phase of the  $AM_3X_8$  compound  $\text{Na}_2\text{Ti}_3\text{Cl}_8$  [26–32].

These studies inspire us to explore 2D multiferroics by searching and manipulating the pattern of the breathing

\*renwei@shu.edu.cn

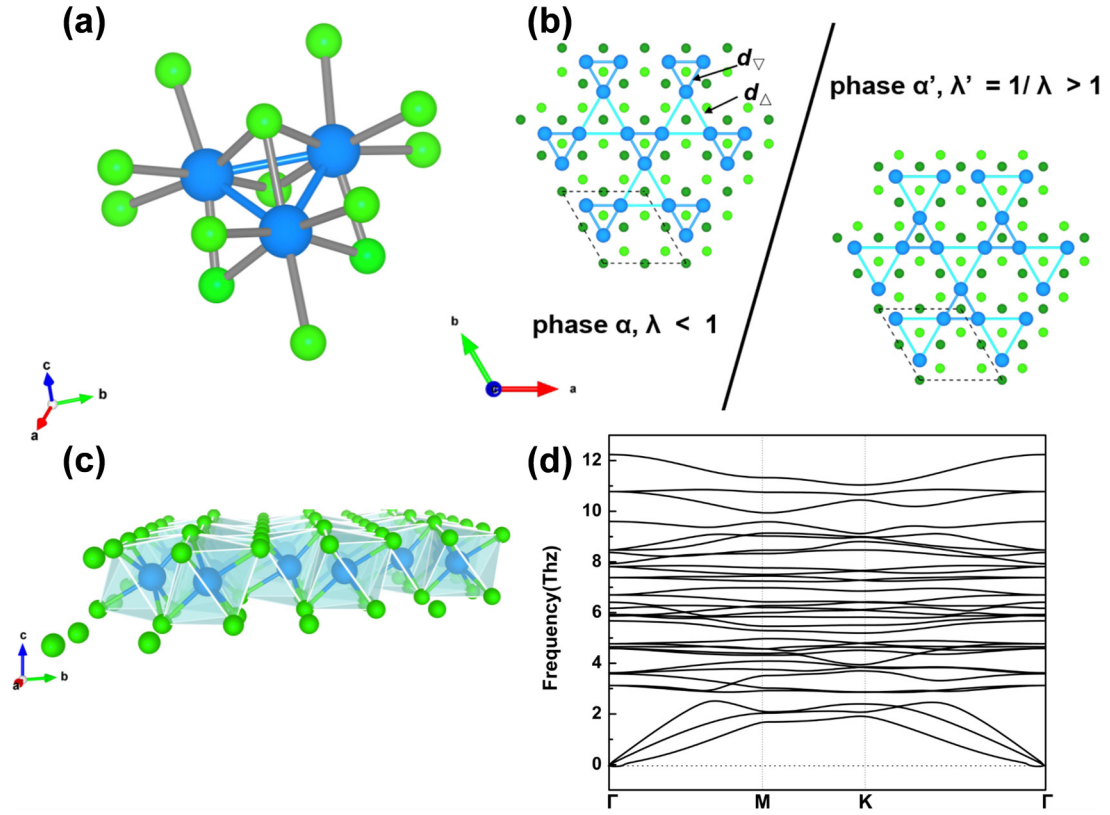


FIG. 1. (a) Perspective view of a  $\text{Ti}_3\text{Cl}_{13}$  (or  $\text{Mo}_3\text{O}_{13}$ , etc.) trimer cluster. (b) The top view of the breathing kagome network for monolayer  $\alpha$ - and  $\alpha'$ - $\text{Ti}_3\text{Cl}_8$ . The unit cell is indicated with dashed lines, the Cl atoms on the top are in light green, and the bottom Cl atoms are in deep green. (c) Perspective view of the monolayer  $\text{Ti}_3\text{Cl}_8$ . (d) Phonon dispersion spectrum for the  $\alpha$  and  $\alpha'$  phases of monolayer  $\text{Ti}_3\text{Cl}_8$ .

kagome lattice. Through first-principles density functional theory calculations, we propose that monolayer titanium halide  $\text{Ti}_3\text{X}_8$  ( $X = \text{Br}$  or  $\text{I}$ ) presents spin-1 breathing kagome magnetic clusters in a 2D multiferroic semiconductor with coexisting FM and FE orders. FE is predicted to stem from structural distortions caused by Ti-atom trimerization that also influence magnetism; this makes it possible to control magnetism by switching the FE polarization. The FE of monolayer  $\text{Ti}_3\text{X}_8$  presents out-of-plane polarization that could be reversed by a vertical electric field causing a “breathing” configurational transformation in the kagome lattice, as shown in Fig. 2. Our calculated magnetic moment is  $2\mu_B$  per trimer cluster, and the ground state is predicted to be FM for  $\text{Ti}_3\text{Br}_8$  and  $\text{Ti}_3\text{I}_8$  with an in-plane easy axis. Two unpaired  $d$  electrons are predicted to be localized on the small trimers, so the magnetic sites are displaced when the direction of FE polarization is switched by an external electric field. These electric and magnetic effects could be extremely useful for stacking and controlling vdW structures, as they manipulate interlayer interactions. Our results further show that, by switching the FE polarization directions of bilayer  $\text{Ti}_3\text{I}_8$ , the magnetic coupling between two layers can be transformed with interlayer FM and AFM orders.

## II. COMPUTATIONAL METHODS

Our calculations were carried out by using the Vienna *ab initio* Simulation Package code (VASP) [33,34]. The generalized gradient approximation (GGA) [35] was used for the

exchange-correlation functional of Perdew-Burke-Ernzerhof (PBE) [36], and the HSE06 hybrid functional [37,38] was also used to check the band gaps. The projector augmented wave method [39] was applied to describe the electron-ion interaction. The kinetic-energy cutoff of the plane-wave basis was set to 600 eV, and a vacuum space of 20 Å was applied. The Monkhorst-Pack  $k$  mesh with  $9 \times 9 \times 1$  was used for geometry relaxation, while  $12 \times 12 \times 1$  was used for single-point energy calculations at these optimized geometries. The vdW correction was considered in relaxation by using the Tkatchenko-Scheffler method with iterative Hirshfeld partitioning [40–42]. Spin-orbit coupling was considered in Dzyaloshinskii-Moriya interaction (DMI) calculations, and the DMI strength was obtained by using a chirality-dependent total energy difference approach [43–45]. Phonon calculations were performed with a  $4 \times 4 \times 1$  supercell and analyzed using the PHONOPY package [46].

## III. RESULTS AND DISCUSSION

### A. Structures

Monolayer titanium halides  $\text{Ti}_3\text{X}_8$  ( $X = \text{Cl}$ ,  $\text{Br}$ , or  $\text{I}$ ) consist of  $\text{Ti}_3\text{X}_{13}$  clusters connected at corners, as shown in Fig. 1 for  $\text{Ti}_3\text{Cl}_8$ . Three edge-sharing distorted  $\text{TiCl}_6$  octahedra form Ti-trimer clusters in which the Ti-Ti distances are slightly shorter than those connecting to the clusters. In this way, the structure forms a breathing kagome Ti-atom network composed of smaller downward pointing equilateral triangles  $\nabla$  and bigger upward pointing equilateral triangles  $\Delta$ . The effect

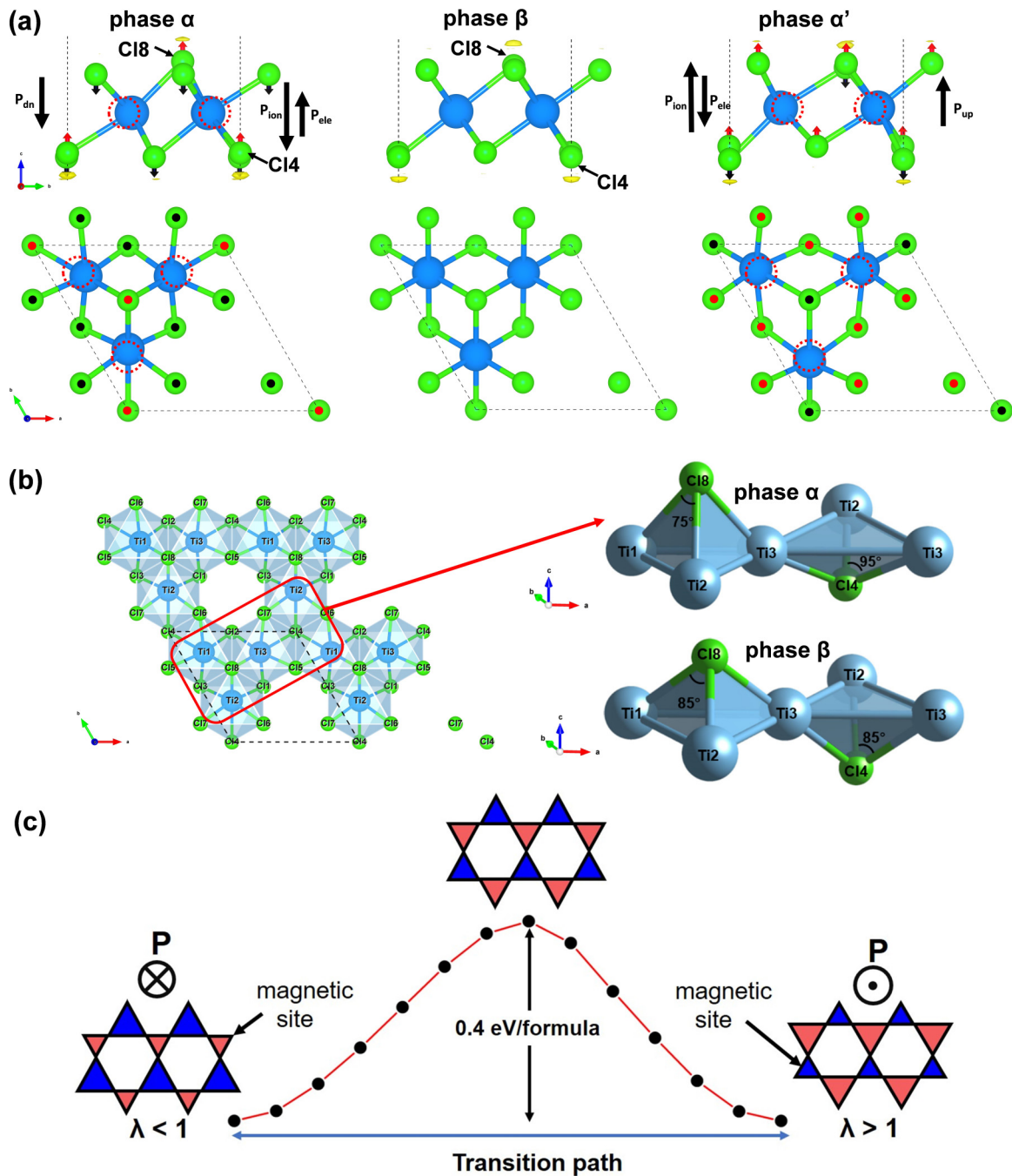


FIG. 2. (a) Side and top views of ferroelectric (FE;  $\alpha$  and  $\alpha'$  phases) and paraelectric (PE;  $\beta$  phase) structures. Ti atoms are in blue, and Cl atoms are in green. The red dashed circles indicate the original ideal positions of the Ti atoms in the PE structure. The red and black arrows (dots) on Cl atoms indicate their upward and downward displacements with respect to Ti atoms. We also show the side-view electron localization function (ELF) of the FE and PE structures (isosurface value of  $0.7967 e/\text{Bohr}^3$ ). The asymmetric electron distribution along the vertical direction indicates the electronic contribution to FE whose polar directions of the ionic and electronic parts are shown. (b) Top view of the  $\alpha$ - $\text{Ti}_3\text{Cl}_8$  and the tetrahedron structures formed by Cl atoms at the top/bottom apex sites and Ti atoms as triangular bases, for phase  $\alpha$  (FE) and phase  $\beta$  (PE). (c) The climbing image nudged elastic band (NEB) result of  $\text{Ti}_3\text{Cl}_8$  for transition path from one FE state to the other bistable state. Two FE states are illustrated by the top views of the breathing kagome networks with different breathing ratios  $\lambda$ . The small triangles represent Ti-trimer magnetic sites.

is quantified by the breathing ratio, defined as  $\lambda = d\nabla/d\Delta$ , where  $d\nabla(d\Delta)$  is the side length of down (up) triangles [24]. The symmetrically equivalent phases are produced, one named  $\alpha$  in which  $\lambda < 1$ , and the other named  $\alpha'$  for which  $\lambda' = 1/\lambda$ .

The calculated lattice constants, the side lengths of cluster triangles, and the breathing ratio parameters are listed in Table I for the phase  $\alpha$ . To check the structural stability of these three  $\text{Ti}_3\text{X}_8$  monolayers, we performed phonon calculations, as seen in Figs. 1(d) and S1 (see Supplemental Material

TABLE I. The lattice constants, the lengths of cluster triangle sides, and the breathing ratios.

Compounds	Lattice constants (Å)	$d\nabla$ (Å)	$d\Delta$ (Å)	Breathing ratios $\lambda$
$\alpha$ -Ti <sub>3</sub> Cl <sub>8</sub>	$a = b = 6.792$	2.996	3.797	0.789
$\alpha$ -Ti <sub>3</sub> Br <sub>8</sub>	$a = b = 7.184$	3.127	4.056	0.771
$\alpha$ -Ti <sub>3</sub> I <sub>8</sub>	$a = b = 7.788$	3.359	4.429	0.758

(SM) [47]). The phonon dispersion spectra show no imaginary frequency over the whole Brillouin zone, demonstrating that the 2D structures are predicted to form stable phases. For  $\lambda = 1$ , the structure takes a high-symmetry form with all equal Ti-Ti distances that the calculations identify as a transition state for the breathing reaction with one imaginary phonon frequency. This unstable paraelectric (PE) transition-state structure is named phase  $\beta$ ; in related materials, it is possible that this structure presents a stable phase, and indeed, this has been reported for V<sub>3</sub>Cl<sub>8</sub> [48].

### B. FE

The structures of the FE phases ( $\alpha$  and  $\alpha'$ ) and PE phase ( $\beta$ ) of the Ti<sub>3</sub>X<sub>8</sub> compounds are shown in Fig. 2. Their internal Ti<sub>3</sub>Cl<sub>13</sub> trimeric cluster units are electrically polarized, like the moiety V<sub>3</sub>O<sub>13</sub> in the polar compound NaSr<sub>2</sub>V<sub>3</sub>O<sub>3</sub>(Ge<sub>4</sub>O<sub>13</sub>)Cl [20], with its dipole moment in the  $\alpha$  and  $\alpha'$  phases originating from the distortion away from the symmetric TiCl<sub>6</sub> octahedra found in the PE phase. For example, in  $\alpha$ -Ti<sub>3</sub>Cl<sub>8</sub>, as illustrated in Fig. 2(a), the Ti atoms move toward the Cl atoms of the top layer, resulting in the distortion of octahedra and the breaking of the inversion symmetry. Thus, in contrast to the PE phase, there appear net dipole moments in the vertical direction of FE phases.

To understand the origin of structural distortion from the PE phase to an FE phase, we compared the different bond lengths and angles [Fig. 2(b)] between the PE and FE structures of Ti<sub>3</sub>Cl<sub>8</sub>. For the upward ClTi<sub>3</sub> tetrahedron of  $\alpha$ , the values of Ti-Ti distances, Ti-Cl-Ti angles, and Ti-Cl bond lengths get smaller, like closing an umbrella. Alternatively, for the downward ClTi<sub>3</sub> tetrahedron, the changes are opposite, like opening an umbrella. To explain such behavior, the electron localization function (ELF) of the FE and PE phases was calculated and shown in Fig. 2(a), where we focus on changes to the electron density in the nonbonding region of the chloride ions away from the Ti-Cl bonds. Electrons deplete on the top side of Cl<sub>8</sub>, making the angles of three Ti-Cl bonds smaller, i.e., 75° in Fig. 2(b); on the other hand, electrons accumulate under the bottom side of Cl<sub>4</sub> with the bigger angle between the three Ti-Cl bonds (95°). Hence, the electric polarization develops in the direction perpendicular to the layer.

The values of polarization are evaluated using the Berry phase method [49,50], and they are 0.016, 0.018, and 0.019 eÅ for Ti<sub>3</sub>Cl<sub>8</sub>, Ti<sub>3</sub>Br<sub>8</sub>, and Ti<sub>3</sub>I<sub>8</sub>, respectively, as listed in Table S1 in the SM [47]. By using the climbing image nudged elastic band (NEB) method [51], we studied the transition path between the two FE states, as shown in Fig. 2(c). The energy barriers of FE direction switching are calculated to be,

respectively, 0.40, 0.44, and 0.32 eV per unit cell for Ti<sub>3</sub>Cl<sub>8</sub>, Ti<sub>3</sub>Br<sub>8</sub>, and Ti<sub>3</sub>I<sub>8</sub>.

### C. Magnetism

In transition-metal compounds, magnetism usually originates from partially occupied  $d$  orbitals, which goes against a traditional requirement of FE for empty  $d$  orbitals in perovskites. In Ti<sub>3</sub>X<sub>8</sub> monolayers, the trimerization of Ti atoms induces FE, and the partially occupied  $d$  orbitals of Ti in Ti<sub>3</sub>X<sub>13</sub> trimer clusters introduce the coexistence of magnetism. The interactions between the Ti atoms in each trimer are so strong that it is not beneficial to assign magnetic moments to each individual atom, and in the following discussion, each Ti-trimer will be considered as one magnetic site. To determine the magnetic ground state, we calculated exchange parameters  $J_1$ ,  $J_2$ , and  $J_3$  using FM and three antiferromagnetic (AFM) configurations, shown in Fig. S2(a) in the SM [47]. In Table II, all  $J$  values of Ti<sub>3</sub>Br<sub>8</sub> and Ti<sub>3</sub>I<sub>8</sub> are positive values, which imply a FM ground state, while Ti<sub>3</sub>Cl<sub>8</sub> shows an AFM ground state with negative  $J$  values. The estimated  $T_C$  results of Ti<sub>3</sub>Br<sub>8</sub> and Ti<sub>3</sub>I<sub>8</sub> by Monte Carlo simulations are 21 and 43 K, respectively, as shown in Fig. S3 in the SM [47]. The magnetic moments of the monolayer Ti<sub>3</sub>X<sub>8</sub> are about  $2\mu_B$  per trimer. The calculations of the magnetic anisotropy energy show that this system has an in-plane easy axis. Furthermore, these three monolayers are all found to be semiconductors (band structures of FM state are shown in Fig. S4 in the SM [47]), and the GGA-PBE (HSE06) band gaps are 0.37, 0.35, and 0.23 eV (1.25, 1.83, and 0.60 eV) for Ti<sub>3</sub>Cl<sub>8</sub>, Ti<sub>3</sub>Br<sub>8</sub>, and Ti<sub>3</sub>I<sub>8</sub>, respectively. Additionally, we calculated the magnetic interaction of the centrosymmetric PE phase; the results suggest that the magnetic ground state is AFM configuration, and the system no longer exhibits trimer local magnetism, as shown in Fig. S2(b) and Table S2 in the SM [47].

For the FE phases, the space-inversion symmetry is broken; thus, the DMI is nonzero. According to Moriya's asymmetry rules [52], the DMI vector  $\mathbf{D}$  is perpendicular to the Ti-I-I-Ti

TABLE II. Magnetic parameters for Ti<sub>3</sub>Cl<sub>8</sub>, Ti<sub>3</sub>Br<sub>8</sub>, and Ti<sub>3</sub>I<sub>8</sub>; positive and negative  $J$  values stand for FM and AFM couplings.

Compounds	$J_1$ (meV)	$J_2$ (meV)	$J_3$ (meV)	$ \mathbf{D} $ (meV)	$ \mathbf{D}_z $ (meV)
Ti <sub>3</sub> Cl <sub>8</sub>	-0.094	-0.014	-0.009	0.057	0.029
Ti <sub>3</sub> Br <sub>8</sub>	0.203	0.018	0.008	0.091	0.046
Ti <sub>3</sub> I <sub>8</sub>	0.463	0.016	0.008	0.151	0.076

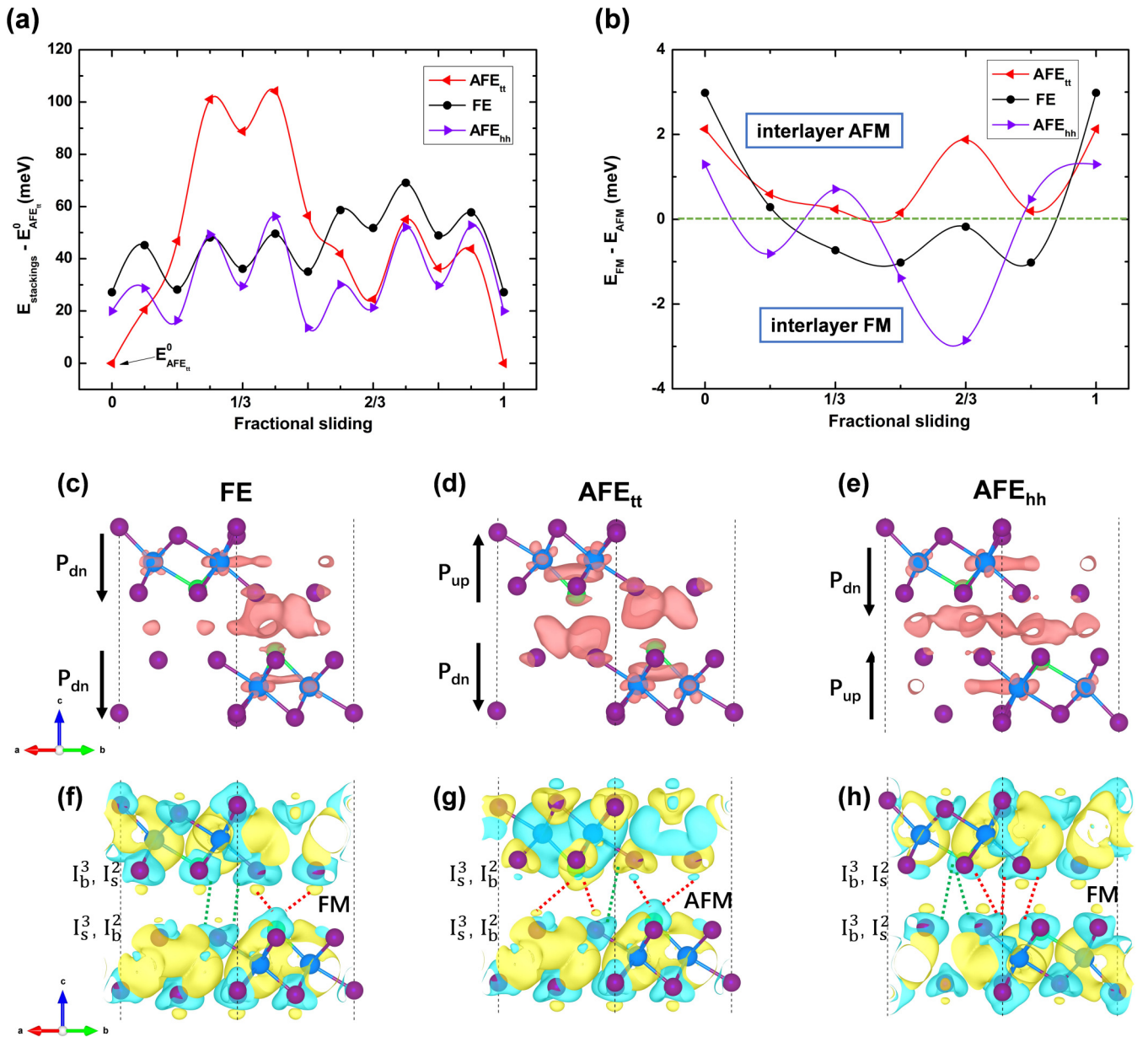


FIG. 3. (a) Stacking energy for ferroelectric (FE), tail-to-tail antiferroelectric ( $\text{AFE}_{tt}$ ), and head-to-head antiferroelectric ( $\text{AFE}_{hh}$ )  $\text{Ti}_3\text{I}_8$  bilayers with the top layer sliding along the  $[1\bar{1}0]$  direction. (b) The energy difference between the interlayer ferromagnetic (FM) and antiferromagnetic (AFM) for  $n/6$  fractional shifting bilayer stackings. (c)–(e) Charge density difference (isosurface value of  $5 \times 10^{-5} e/\text{Bohr}^3$ ) for  $\frac{2}{3}$ -FE,  $\text{AFE}_{tt}$ , and  $\text{AFE}_{hh}$  stackings, indicating charge accumulation. (f)–(h) Spin density with isosurface value of  $3 \times 10^{-4} e/\text{Bohr}^3$  for interlayer magnetic ground state; the yellow and blue represent spin-up and spin-down, respectively. The shortest I-I distances are marked by red dotted lines, and the second shortest I-I distances are marked by green dotted lines.

plane in the big triangle (in the middle of three Ti-trimers; see Fig. S5 in the SM [47]). The in-plane components of  $\mathbf{D}$  cancel each other out, leaving only the out-of-plane component  $\mathbf{D}_z$ , and the directions of  $\mathbf{D}_z$  are opposite for the two FE structures. The values of  $\mathbf{D}$  and  $\mathbf{D}_z$  are listed in Table II. One could see that the DMI strength of monolayer  $\text{Ti}_3\text{I}_8$  is comparable with the second-nearest  $\mathbf{D}_2$  in monolayer  $\text{CrI}_3$  and the nearest  $\mathbf{D}_1$  in Janus monolayer  $\text{Cr}(\text{I}, \text{Cl})_3$  [53]. Therefore, the direction switching of FE polarization could change the overall direction of  $\mathbf{D}$  (or  $\mathbf{D}_z$ ).

#### D. Bilayers

Since the magnetic moments are localized on the small triangles (trimers) in the breathing kagome network, the positions of magnetic sites may change with the breathing. As a result, by switching the polarization direction, we can make an in-plane displacement of the position of magnetic sites. This could introduce functionality into 2D vdW systems via controlling stacking orders or patterns of various layered structures. In bilayer  $\text{CrI}_3$ , the magnetic ground state can be tuned between interlayer AFM and FM by changing

the stacking order [54]. Here, the 2D  $\text{Ti}_3\text{X}_8$  can serve as an excellent functional layer combining FE and FM, such that applying an external field can not only achieve the reversal of FE polarization but also magnetic control, with the nonvolatile property preserved after removal of the external field.

We choose bilayer  $\text{Ti}_3\text{I}_8$  (Fig. S6 in the SM [47]) for the case study of interlayer magnetism from the strong I atom  $p$  orbital wave function extension. Besides the FE interlayer AA stacking, we consider the tail-to-tail antiferroelectric ( $\text{AFE}_{\text{tt}}$ ) and head-to-head antiferroelectric ( $\text{AFE}_{\text{hh}}$ ) bilayer stackings with opposite FE directions. For these three stackings, we shift the top layer with respect to the bottom layer along the  $[1\bar{1}0]$  direction to study the stacking energy, as shown in Fig. S6 in the SM [47]. Fig. 3(a) shows the stacking energy after stacking-constrained relaxation (the lowest stacking energy  $E_{\text{AFE}_{\text{tt}}}^0$  is set to 0). The results show that the stackings with the  $n/6$  fractional shifts are at local minima (except for  $\frac{1}{6}$ - $\text{AFE}_{\text{tt}}$  and  $\frac{1}{2}$ - $\text{AFE}_{\text{tt}}$ ), which indicates that these stackings are experimentally possible as for bilayer  $\text{CrI}_3$ . Next, we performed fully structural optimization of  $n/6$  fractional shift structures with interlayer FM and AFM configurations, which still maintain the original stackings (except for  $\frac{1}{6}$ - $\text{AFE}_{\text{tt}}$  and  $\frac{1}{2}$ - $\text{AFE}_{\text{tt}}$ ), further proving the feasibility of these stackings. The interlayer magnetic exchange energy of these stackings, defined as the energy difference between the interlayer FM and AFM, is shown in Fig. 3(b). The results demonstrate that interlayer magnetic configurations can be transformed between FM and AFM by either interlayer sliding or FE polarization reversal of one or both layers.

We then carefully studied the magnetic coupling between two layers [55,56], which is mainly contributed by exchange interaction of I atoms between interlayer Ti-trimers. Firstly, we analyzed the structure and spin density of the monolayer  $\text{Ti}_3\text{I}_8$ , as shown in the Fig. S7 in the SM [47]. Then for  $\frac{2}{3}$  stacking, there is an interlayer FM  $\rightarrow$  AFM  $\rightarrow$  FM transition when an FE  $\rightarrow$   $\text{AFE}_{\text{tt}}$   $\rightarrow$   $\text{AFE}_{\text{hh}}$  switching occurs. We demonstrate charge density difference and spin density to investigate the interlayer magnetic coupling transition mechanism. For FE, in Fig. 3(c), we focus on the exchange between one trimer at the bottom and the nearest-neighbor in the top layer (shown in Fig. S6 in the SM [47]), the charge accumulation mainly occurs at  $\text{I}_s^3$ - $\text{I}_s^2$  (4.11 Å, the shortest I-I) and  $\text{I}_b^2$ - $\text{I}_s^2$  (4.47 Å, the second shortest I-I). In the case of interlayer AFM, the direct exchange of  $\text{I}_s^3$ - $p$  to minor  $\text{I}_s^2$ - $p_z$  dominates, while the direct exchange of  $\text{I}_b^2$ - $p_{x/y}$  to  $\text{I}_s^2$ - $p_{x/y}$  dominates in the interlayer-FM case. Although the exchange strength of  $\text{I}_s^3$ - $\text{I}_s^2$  is greater than that of  $\text{I}_b^2$ - $\text{I}_s^2$ , the total of 12  $\text{I}_b^2$ - $\text{I}_s^2$  channels is slightly stronger than the total of 3  $\text{I}_s^3$ - $\text{I}_s^2$  channels, making the interlayer FM energy 0.18 meV/cell lower.

When FE is switched to  $\text{AFE}_{\text{tt}}$ , the position and structures of top layer interlayer-I atom variations lead to the changes in the magnetic exchange as well. The charge accumulation mainly occurs at  $\text{I}_s^3$ - $\text{I}_b^2$  (4.24 Å, the shortest I-I), where the direct exchange between  $\text{I}_s^3$ - $p$  and  $\text{I}_b^2$ - $p_{x/y}$  causes the interlayer AFM. The second shortest  $\text{I}_b^2$ - $\text{I}_b^2$  reaches 4.64 Å, making the exchange interaction between  $\text{I}_b^2$ - $p_{x/y}$  and  $\text{I}_b^2$ - $p_{x/y}$  much weaker, resulting an interlayer FM. Therefore, the interlayer AFM is 1.88 meV/cell lower than the interlayer FM. As for  $\text{AFE}_{\text{hh}}$  stacking, interlayer I-I interactions are another story. The charges are mainly accumulated at  $\text{I}_s^2$ - $\text{I}_s^2$  (4.29 Å, the shortest I-I) and  $\text{I}_b^3$ - $\text{I}_s^2$  (4.51 Å, the second shortest I-I). The direct exchange from  $\text{I}_s^2$ - $p_{x/y}$  to  $\text{I}_s^2$ - $p_{x/y}$  makes the nearest bottom Ti-trimer and top Ti-trimer FM ordered, also the direct exchange from  $\text{I}_b^3$ - $p_{x/y}$  to  $\text{I}_s^2$ - $p_{x/y}$  makes the second nearest bottom Ti-trimer and top Ti-trimer FM ordered as well. Hence, the interlayer FM energy is lower by 2.86 meV/cell. For  $\frac{1}{3}$  and 0 stacking, the interlayer magnetic couplings are described in detail in Figs. S8 and S9 in the SM [47]. Based on the above studies, the interlayer magnetism can be modulated by sliding the bilayer or switching the direction of FE.

#### IV. CONCLUSIONS

In conclusion, we predicted a 2D intrinsic FE/FM semiconductor  $\text{Ti}_3\text{X}_8$  ( $X = \text{Br}$  or  $\text{I}$ ) whose mechanism of breathing kagome lattice patterns correspond to two opposite out-of-plane FE polarizations. The cluster magnets annihilate and generate simultaneously at neighboring sites as the kagome lattice transforms between two polar configurations, and such a displacement of the magnetic sites can be realized by switching the direction of FE polarization. In bilayer  $\text{Ti}_3\text{I}_8$ , we found that the interlayer magnetic coupling can be tuned between FM and AFM by changing the polarization directions. This exotic and functional property provides potential magnetoelectric applications for vdW layered structures to be manipulated by switching of FE polarization.

#### ACKNOWLEDGMENTS

This paper was supported by the National Natural Science Foundation of China (Grants No. 51861145315, No. 11929401, No. 12074241, No. 11804216), the Independent Research and Development Project of State Key Laboratory of Advanced Special Steel, Shanghai Key Laboratory of Advanced Ferrometallurgy, Shanghai University (Grant No. SKLASS 2020-Z07), the Science and Technology Commission of Shanghai Municipality (Grants No. 19DZ2270200, No. 19010500500, No. 20501130600), and High Performance Computing Center, Shanghai University.

- [1] R. Ramesh and N. A. Spaldin, *Nat. Mater.* **6**, 21 (2007).
- [2] W. Eerenstein, N. D. Mathur, and J. F. Scott, *Nature (London)* **442**, 759 (2006).
- [3] I. B. Bersuker, *Phys. Rev. Lett.* **108**, 137202 (2012).
- [4] S. Dong, J.-M. Liu, S.-W. Cheong, and Z. Ren, *Adv. Phys.* **64**, 519 (2015).

- [5] N. A. Spaldin, S.-W. Cheong, and R. Ramesh, *Phys. Today* **63**(10), 38 (2010).
- [6] J. T. Heron, J. L. Bosse, Q. He, Y. Gao, M. Trassin, L. Ye, J. D. Clarkson, C. Wang, J. Liu, S. Salahuddin, D. C. Ralph, D. G. Schlom, J. Íñiguez, B. D. Huey, and R. Ramesh, *Nature (London)* **516**, 370 (2014).

- [7] P. Rovillain, R. de Sousa, Y. Gallais, A. Sacuto, M. A. Méasson, D. Colson, A. Forget, M. Bibes, A. Barthélémy, and M. Cazayous, *Nat. Mater.* **9**, 975 (2010).
- [8] J. B. Neaton, C. Ederer, U. V. Waghmare, N. A. Spaldin, and K. M. Rabe, *Phys. Rev. B* **71**, 014113 (2005).
- [9] T. Choi, S. Lee, Y. J. Choi, V. Kiryukhin, and S.-W. Cheong, *Science* **324**, 63 (2009).
- [10] T. Kimura, T. Goto, H. Shintani, K. Ishizaka, T. Arima, and Y. Tokura, *Nature (London)* **426**, 55 (2003).
- [11] M. Kenzelmann, A. B. Harris, S. Jonas, C. Broholm, J. Schefer, S. B. Kim, C. L. Zhang, S. W. Cheong, O. P. Vajk, and J. W. Lynn, *Phys. Rev. Lett.* **95**, 087206 (2005).
- [12] J. S. Zhang, Y. Xie, X. Q. Liu, A. Razpopov, V. Borisov, C. Wang, J. P. Sun, Y. Cui, J. C. Wang, X. Ren, H. Deng, X. Yin, Y. Ding, Y. Li, J. G. Cheng, J. Feng, R. Valentí, B. Normand, and W. Yu, *Phys. Rev. Res.* **2**, 013144 (2020).
- [13] V. Borisov, S. Biswas, Y. Li, and R. Valentí, *Phys. Status Solidi B* **256**, 1900229 (2019).
- [14] B. Huang, G. Clark, E. Navarro-Moratalla, D. R. Klein, R. Cheng, K. L. Seyler, D. Zhong, E. Schmidgall, M. A. McGuire, D. H. Cobden, W. Yao, D. Xiao, P. Jarillo-Herrero, and X. Xu, *Nature (London)* **546**, 270 (2017).
- [15] C. Gong, L. Li, Z. Li, H. Ji, A. Stern, Y. Xia, T. Cao, W. Bao, C. Wang, Y. Wang, Z. Q. Qiu, R. J. Cava, S. G. Louie, J. Xia, and X. Zhang, *Nature (London)* **546**, 265 (2017).
- [16] K. Chang, J. Liu, H. Lin, N. Wang, K. Zhao, A. Zhang, F. Jin, Y. Zhong, X. Hu, W. Duan, Q. Zhang, L. Fu, Q.-K. Xue, X. Chen, and S.-H. Ji, *Science* **353**, 274 (2016).
- [17] J. R. Reimers, S. A. Tawfik, and M. J. Ford, *Chem. Sci.* **9**, 7620 (2018).
- [18] W. Ding, J. Zhu, Z. Wang, Y. Gao, D. Xiao, Y. Gu, Z. Zhang, and W. Zhu, *Nat. Commun.* **8**, 14956 (2017).
- [19] Y. Zhou, D. Wu, Y. Zhu, Y. Cho, Q. He, X. Yang, K. Herrera, Z. Chu, Y. Han, M. C. Downer, H. Peng, and K. Lai, *Nano Lett.* **17**, 5508 (2017).
- [20] L. D. Sanjeewa, M. A. McGuire, C. D. McMillen, V. O. Garlea, and J. W. Kolis, *Chem. Mater.* **29**, 1404 (2017).
- [21] J. P. Sheckelton, J. R. Neilson, D. G. Soltan, and T. M. McQueen, *Nat. Mater.* **11**, 493 (2012).
- [22] M. Mourigal, W. T. Fuhrman, J. P. Sheckelton, A. Wartelle, J. A. Rodriguez-Rivera, D. L. Abernathy, T. M. McQueen, and C. L. Broholm, *Phys. Rev. Lett.* **112**, 027202 (2014).
- [23] R. Flint and P. A. Lee, *Phys. Rev. Lett.* **111**, 217201 (2013).
- [24] A. Akbari-Sharraf, R. Sinclair, A. Verrier, D. Ziat, H. D. Zhou, X. F. Sun, and J. A. Quilliam, *Phys. Rev. Lett.* **120**, 227201 (2018).
- [25] J. P. Sheckelton, F. R. Foronda, L.-D. Pan, C. Moir, R. D. McDonald, T. Lancaster, P. J. Baker, N. P. Armitage, T. Imai, S. J. Blundell, and T. M. McQueen, *Phys. Rev. B* **89**, 064407 (2014).
- [26] N. Hänni, M. Frontzek, J. Hauser, D. Cheptiakov, and K. Krämer, *Z. Anorg. Allg. Chem.* **643**, 2063 (2017).
- [27] Y. Haraguchi, C. Michioka, M. Ishikawa, Y. Nakano, H. Yamochi, H. Ueda, and K. Yoshimura, *Inorg. Chem.* **56**, 3483 (2017).
- [28] A. Paul, C. M. Chung, T. Birol, and H. J. Changlani, *Phys. Rev. Lett.* **124**, 167203 (2020).
- [29] Z. A. Kelly, T. T. Tran, and T. M. McQueen, *Inorg. Chem.* **58**, 11941 (2019).
- [30] S. Oh, K. H. Choi, S. Chae, B. J. Kim, B. J. Jeong, S. H. Lee, J. Jeon, Y. Kim, S. S. Nanda, L. Shi, D. K. Yi, J.-H. Lee, H. K. Yu, and J.-Y. Choi, *J. Alloys Compd.* **831**, 154877 (2020).
- [31] P. Z. S. N. Magonov, H. Rotter, H. J. Cantow, G. Thiele, J. Ren, and M. H. Whangbo, *J. Am. Chem. Soc.* **115**, 2495 (1993).
- [32] J. P. Sheckelton, K. W. Plumb, B. A. Trump, C. L. Broholm, and T. M. McQueen, *Inorg. Chem. Front.* **4**, 481 (2017).
- [33] G. Kresse and J. Hafner, *Phys. Rev. B* **48**, 13115 (1993).
- [34] G. Kresse and J. Furthmüller, *Comput. Mater. Sci.* **6**, 15 (1996).
- [35] S. Grimme, *J. Comput. Chem.* **27**, 1787 (2006).
- [36] J. P. Perdew, K. Burke, and M. Ernzerhof, *Phys. Rev. Lett.* **77**, 3865 (1996).
- [37] A. V. Krukau, O. A. Vydrov, A. F. Izmaylov, and G. E. Scuseria, *J. Chem. Phys.* **125**, 224106 (2006).
- [38] J. Heyd and G. Scuseria, *J. Chem. Phys.* **118**, 8207 (2003).
- [39] G. Kresse and D. Joubert, *Phys. Rev. B* **59**, 1758 (1999).
- [40] T. Bučko, S. Lebègue, J. Hafner, and J. G. Ángyán, *J. Chem. Theory Comput.* **9**, 4293 (2013).
- [41] T. Bucko, S. Lebègue, J. G. Ángyán, and J. Hafner, *J. Chem. Phys.* **141**, 034114 (2014).
- [42] P. Bultinck, C. Van Alsenoy, P. W. Ayers, and R. Carbo-Dorca, *J. Chem. Phys.* **126**, 144111 (2007).
- [43] J. Liang, W. Wang, H. Du, A. Hallal, K. Garcia, M. Chshiev, A. Fert, and H. Yang, *Phys. Rev. B* **101**, 184401 (2020).
- [44] H. Yang, A. Thiaville, S. Rohart, A. Fert, and M. Chshiev, *Phys. Rev. Lett.* **115**, 267210 (2015).
- [45] H. Yang, G. Chen, A. A. C. Cotta, A. T. N'Diaye, S. A. Nikolaev, E. A. Soares, W. A. A. Macedo, K. Liu, A. K. Schmid, A. Fert, and M. Chshiev, *Nat. Mater.* **17**, 605 (2018).
- [46] A. Togo and I. Tanaka, *Scr. Mater.* **108**, 1 (2015).
- [47] See Supplemental Material at <http://link.aps.org/supplemental/10.1103/PhysRevB.104.L060405> for further details, which includes Ref. [56]. Phonon dispersion spectra, band structures for monolayer  $Ti_3X_8$  ( $X = Cl, Br, \text{ or } I$ ), magnetic configurations when calculating magnetic parameters and two other bilayer  $Ti_3I_8$  stackings.
- [48] H. Xiao, X. Wang, R. Wang, L. Xu, S. Liang, and C. Yang, *Phys. Chem. Chem. Phys.* **21**, 11731 (2019).
- [49] R. Resta, *Rev. Mod. Phys.* **66**, 899 (1994).
- [50] R. D. King-Smith and D. Vanderbilt, *Phys. Rev. B* **47**, 1651 (1993).
- [51] S. Smidstrup, A. Pedersen, K. Stokbro, and H. Jonsson, *J. Chem. Phys.* **140**, 214106 (2014).
- [52] T. Moriya, *Phys. Rev.* **120**, 91 (1960).
- [53] C. Xu, J. Feng, S. Prokhorenko, Y. Nahas, H. Xiang, and L. Bellaiche, *Phys. Rev. B* **101**, 060404(R) (2020).
- [54] N. Sivadas, S. Okamoto, X. Xu, C. J. Fennie, and D. Xiao, *Nano Lett.* **18**, 7658 (2018).
- [55] P. Jiang, C. Wang, D. Chen, Z. Zhong, Z. Yuan, Z.-Y. Lu, and W. Ji, *Phys. Rev. B* **99**, 144401 (2019).
- [56] C. Wang, X. Zhou, L. Zhou, Y. Pan, Z.-Y. Lu, X. Wan, X. Wang, and W. Ji, *Phys. Rev. B* **102**, 020402(R) (2020).